EFFECT OF CITRATE AND GLUTAMATE IONS ON THE PRECIPITATION OF HYDROXYLAPATITE: SYNTHESIS AND CHARACTERIZATION THROUGH XRD, FTIR, SAXS, AND ICP-AES

GIULIO ISACCO LAMPRONTI
Dipartimento di Scienze della Terra, Università di Firenze, Via La Pira 4, I-50121 Firenze

INTRODUCTION

Synthetic HAp, as well as other calcium phosphates, is widely used in various biomedical applications (ceramics, cements, etc.) because of its excellent biocompatibility and surface active properties with living tissues. Nanocrystalline HAp powders are generally produced at low-near room temperature by wet methods or sol-gel synthesis (Gross & Berndt, 2002; Ferraz *et al*., 2004). At low temperatures HAp crystals precipitate with acicular or plate-like shape with the lowest dimension usually smaller than 10 nm. It is generally known that temperature, pH, dropping rate, and ripening time (Pang & Bao, 2003; Sàenz *et al*., 2003; Van der Houwen, 2003; Landi *et al*., 2004; Liu *et al*., 2006) all affect Ca/P as well as crystallinity of the precipitating crystals: as an example, a stoichiometric HAp can be obtained by ripening for 5 hours at 90° and *p*H = 10 (Rodrìguez-Lorenzo & Vallet-Regì, 2000).

Addition of organic ligands in the synthesis of HAp by wet methods is a common technique, with a marked tendency to use organic compounds characterized by carboxylate groups (Hunter *et al*., 1996; Matsumoto *et al*., 2002; Van der Houwen *et al*., 2003; Wang *et al*., 2006; Boanini *et al*., 2006) because of their ease to bind HAp surface. In the present work two carboxylated ligands were used: glutamic acid, $C_5H_9NO_4$, and citric acid, $C_6H_8O_7$.

In the human body glutamate is found as part of macromolecules such as proteins involved in the biomineralization process (Hunter *et al*., 1996). The *in vitro* studies of Boanini *et al*. (2006) and Tsortos & Nancollas (2002) suggest that glutamate is an inhibitor to HAp formation.

The content of citric acid in mineralized tissues can be as high as 1 wt.% (Biltz *et al*., 1969) and it is likely to be linked to HAp crystals through its carboxylate groups –COOH (Elliott, 2002). Citric acid is known to be an inhibitor in HAp precipitation experiments (Brečević & Füredi Milhofer, 1979; Weng *et al*., 2002a; 2002b; Van der Houwen, 2003; Van der Houwen *et al*., 2003); citric acid is suspected to bind to the $\{1\,-1\,2\,1\}$ and $\{1\,0\,-1\,0\}$ surfaces than to $\{0\,0\,0\,1\}$, inhibiting the growth along the former ones (Filgueiras *et al*., 2006).

The focus of this study was to determine the effects of citrate and glutamate on nanocrystalline HAp precipitation. This involved finding a wet method to produce nanocrystalline powders. Although the effect of citrate and glutamate have been studied in the literature, results are still at a preliminary stage: it is not clear which is the effect of their presence on the first moments of HAp nucleation in solution, which is their effect as a function of their concentration and whether it is indeed possible to characterize the precipitated powder so that we can think an application beyond the scientific interest. A large part of the present work concentrates on microstructural characterization of the products. On one hand we tried to improve the treatment of data collected with conventional techniques (XRD, FTIR): specifically diffraction data were refined with Rietveld method that is not common on nanocrystalline powders using a conventional X-ray source. On the other hand we associated with these traditional techniques the analytical SAXS technique with conventional X-ray source, never tested before on synthetic HAp

powders. The main objective was to find significative microstructural variables to quantitatively determine the effect of the used ligands on the produced nanocrystalline powders.

EXPERIMENTAL METHODS: SYNTHESIS

Direct precipitation of HAp occurred by mixing aqueous solutions of 14.5 mM $CaCl_2 \cdot 2H_2O$ and 8.7 mM $Na_2HPO_4 \cdot 10H_2O$. Both solutions contained 0.1 M NaCl and were buffered to a *p*H of 7.4 using Tris(hydroxy)methilaminomethane and HCl. The resulting solutions possessed an initial Ca^{2+}/PO_4^{3-} ratio of 1.67, equivalent to that of stoichiometric HAp. After remaining in contact with the solution for 330 minutes at 25°C and with constant stirring, the precipitates were centrifuged for 10 minutes, washed with deionized water, and dried overnight at T = 37°C. The effect of different organic ligands was studied by adding citrate or L-glutamate to the phosphate solution. The concentrations organic ligands used were 0.00 mM (control samples, CO), 0.01 mM (CIL and GLL samples), 0.10 mM (CI and GL samples) and 1.00 mM (CIH and GLH samples). All the experiments were performed in triplicates to check reproducibility.

EXPERIMENTAL METHODS: CHARACTERIZATION

ICP-AES

An ICP-AES Varian VISTA PRO was used to measure both calcium and phosphorus. Calcium was measured at wavelengths of 315.887 and 317.933, while phosphorus at 178.222 and 213.618 nm, at concentrations higher than 2 mg/l and lower than 20 mg/l for both elements. Standards were prepared using MERCK standards of 10,000 mg/l calcium and phosphorus. Five standard solutions were used at concentrations of 1, 2.5, 5, 10 and 20 mg/l to calculate a calibration curve for both calcium and phosphorus (correlation index $R \geq 0.990$, typical Relative Standard Deviation for each data point between 0.4 and 1%).

SEM

Scanning Electron Microscopy (SEM) imaging was performed using a Philips XL30 microscope operating with a beam voltage of 5 kV and spot size 3 μm. Small amounts of sample were dispersed in deionized water using an ultrasonic bath for 10 min. HAP crystallites from the resulting suspension were evaporatively deposited on to a carbon-coated copper grid. This grid was then attached to an aluminium stub and gold coated (5 nm coating).

XRD

X-ray powder diffraction (XRD) patterns were obtained using an Enraf Nonius diffractometer fitted with a 120° curved position sensitive detector (PSD, 4096 channels over 120°, with a resolution of 0.03°) and fixed beam-sample detector geometry working with a Cu Ka_1 radiation. LaB_6 was used as internal standard to calibrate the collected patterns and to evaluate the instrumental broadening.

FTIR

FTIR spectra were collected between 4000 and 400 cm^{-1} using 12 scans with a resolution of 1 cm^{-1} using a Philips PU 9800 FTIR spectrophotometer whose sample chamber was purged with dry air. 0.9 mg (±0.02) of the powdered samples was carefully mixed with 200 mg (± 1) of KBr (infrared grade) and pelletized under a pressure of 10 tons / 531 mm^2 for 1 minute. The FTIR spectrum obtained for a KBr

pellet of 200 mg was used as background, to subtract the influence of the analytical conditions from the FTIR spectra of the sample. The interferogram obtained is automatically transformed into an FTIR spectrum. The FTIR spectra obtained from the samples were automatically corrected by deducting the spectrum of the background from the absorption spectra of the sample.

The FTIR spectra obtained were processed using the commercial program GRAMS/32. Selected areas were baseline subtracted using a cubic function and corrected for offset.

SAXS

Small Angle X-ray Scattering (SAXS) experiments were performed using the Bruker AXS NanoSTAR facility at Cardiff University with a fixed sample-to-detector distance of 1.25 m. Approximately 10 mg of mixed HAp powder from three analogous experiments were loaded into the sample holder between two mica sheets and attached to the sample stage. The sample chamber was placed under a vacuum and data were collected for 90 minutes. The data were corrected for camera distortions and a background image subtracted. The two-dimensional detector output was converted into spherically averaged one-dimensional profiles. Hence values for crystal thickness (T) of the smallest dimension can be determined from the SAXS data, a method often referred to as 1-dimensional SAXS (Hiller & Wess, 2006).

Basically we need two quantities, the Porod constant, P, and the Porod invariant, Q:

$$lim_{q\to\infty} I(q)q^4 = (N / V)\, 2\pi\, \Delta\rho^2\, S = 2\pi\sigma = P \qquad (1)$$

$$\int_0^\infty I(q)q^2\, \mathrm{d}q = (N / V)\, 2\pi^2\, v\, (1\text{-}v) = Q \qquad (2)$$

where N / V is the particle number density, $\Delta\rho$ is the elctron density difference between the scattering objects and the surrounding medium and works as a scale factor, S is the surface of one particle (Porod, 1982; Vachette & Svergun, 2002), V denotes the volume per particle, and v is the volume fraction of the mineral phase, and 1-v is the volume fraction of the sorrounding medium Fratzl *et al*. (1996a; 1996b).

A "thickness" value T can be calculated from the ratio:

$$(4Q) / (\pi P) = [4\, v\, (1\text{-}v)] / \sigma = T \qquad (3)$$

Assuming $v = 0.5$ (as it is in bones) and crystals with H (height) $\leq L$ (length) $\leq W$ (width),

$$T \approx 1 / [(1/H) + (1/L) + (1/W)]$$
Plates: $T = H$
Needles: $H / 2$
Cubes: $H / 3$ (4)

In order to compare differences in shape between patterns, the plots need to be rescaled and normalized to account for different crystallite sizes. Fratzl *et al.* (1996a; 1996b) defined a dimensionless variable $x = qT$ and the function:

$$G(x) = (4\, x^3\, I) / (\pi\, P\, T^5) \qquad (5)$$

which is normalized to $\int_0^\infty G(x)\mathrm{d}x = 1$. This function can give some indication about the typical shape of the crystals. In particular, it would have its maximum at $x = 0$ if there were randomly distributed plate-like crystals in the collagen fibrils. In the case of randomly distributed needle-like crystals, $G(x)$ would

increase linearly at small x, exhibit a maximum at some finite x, and then decrease like x^{-2} at large x values.

DATA ANALYSIS

SEM

Scanning electron microscopy (Fig. 1) showed that the crystallites were either rod- or plate-like, with one dimension (tens of nanometers) much longer than the other two.

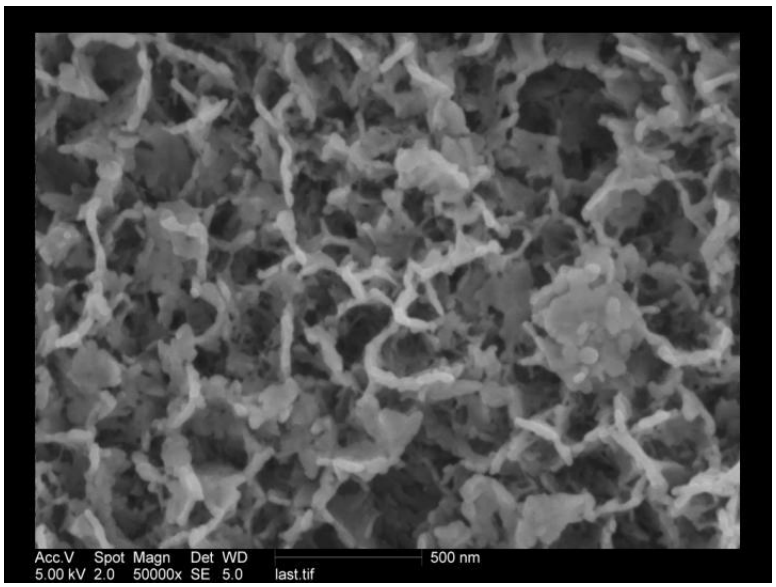

Fig. 1 – SEM micrograph of control sample.

XRD

The XRD patterns (Fig. 2a) showed that all the synthetic powders were pure HAp with no evidence for the presence of any amorphous phases. The precipitated crystals can be classified as *Ca-deficient hydoxyapatite*, due to the low Ca/P ratio from ICP-AES analysis, ranging from 1.45 to 1.50. The inhibiting role of the citrate and glutamate ligands on HAp crystallization resulted in a broadening of the X-ray diffraction peaks. Peak broadening is often experimentally measured as integral breadth (peak area / peak height) and relates to "crystallinity", a combination of crystallites size and lattice strain. The lattice strain is a deviation of the interplanar distance with respect to that of a strain free crystal ($\varepsilon(d) = \Delta d / d$). In order to measure these parameters simultaneously a Rietveld refinements of the XRD data were performed using MAUD software

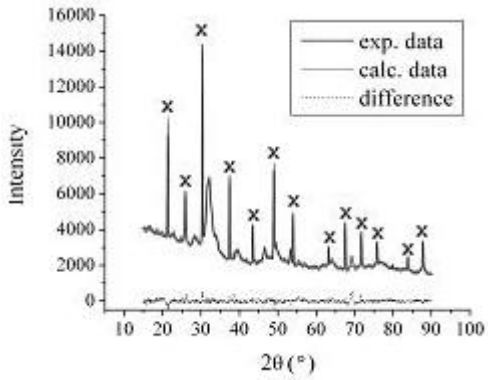

Fig. 2a – Experimental (grey solid line) and calculated (black solid line) powder pattern (Rwp = 2.9%) for CO1. The lower trace is the difference between observed and calculated patterns, LaB_6 peaks are marked with a cross. The interval around 2θ = 67° is affected by a defect in the detector and it was excluded by the refinement.

(Lutterotti, 2006) and applying the Popa model for size and strain (Popa, 1998). As HAp has hexagonal symmetry with a space group of $P6_3/m$, the peak broadening model treats the crystallites as hexagonal prisms.

The estimated crystallites size (nm) and strain and calculated integral breadth (in radians) along *a* and *c* are shown in Fig. 2b.

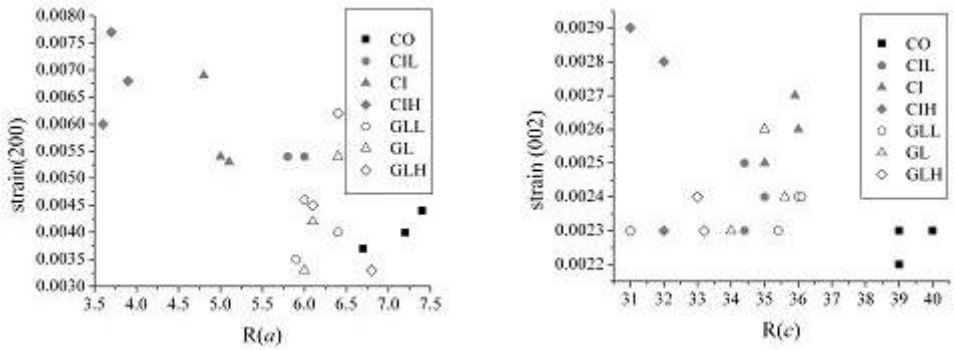

Fig. 2b – Microstructural parameters from the Rietveld refinements: R(*a*) = crystal length along *a*; R(*c*) = crystal length along *c*; strain (002) = lattice strain for peak (002). Goodness-of-fit indexes c^2 were always < 2.5 and mostly < 2. Three and four parameters were refined respectively for size and strain. All standard deviation were < 3% for size parameters, < 5% for strain parameters.

FTIR

FTIR spectrum of sample CIH1 is shown in Fig. 3a. All samples showed carbonate impurities relating to the CO_3^{2-} normal mode ν_2 in the range 850-880 cm^{-1} (Rey *et al*., 1990) Fourier deconvolution and second-derivative analysis (Fig. 3b) indicated carbonate in tetrahedral site (B Type substitution) and no evidence for carbonate substitution for OH^- (A Type substitution); presence of $[PO_3(OH)]^{2-}$ tetrahedra was also detected (Fig. 3c). Bands at 1415 cm^{-1} and H_2O bending mode peak at 1640 cm^{-1} increased in HAp samples crystallized in the presence of citrate. These features should relate to a surface complex (Lackovic *et al*., 2003) rather than an incorporation of citrate in the HAp structure, and not to an increase in the carbonate concentration within these samples.

FTIR analysis can also provide a crystallinity index through the addition of the intensities of the two PO_4^{3-} normal mode (ν_4) peaks (at 603 and 563 cm^{-1}) divided by the absolute intensity of the valley between them (Wright & Schartz, 1995; Surovel & Stiner, 2001). Fig. 4 shows the graphical correlation FTIR analysis can also provide a crystallinity index through the addition of the between these values and the integral breadth as calculated for the 200 peak from XRD patterns refinements. While there was a good correlation between the FTIR and XRD data for HAp synthesized in the presence of citrate, there is no apparent change in the

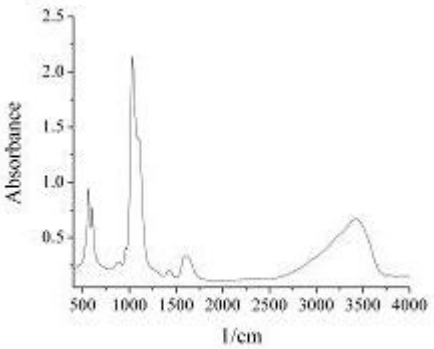

Fig. 3a – FTIR spectrum of sample CIH1.

FTIR crystallinity index of the HAp synthesized glutamate as a function of the ligand concentration.

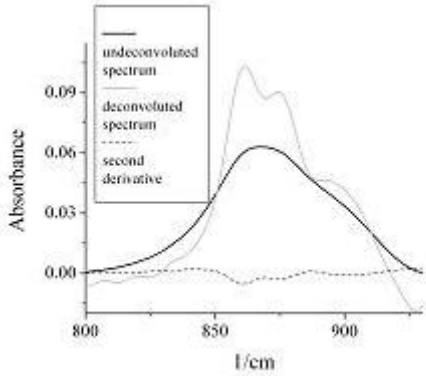

Fig. 3b – Undeconvoluted, deconvoluted and second derivative spectra of sample CO_2 in the CO_3^{2-} bending mode ν_2 region.

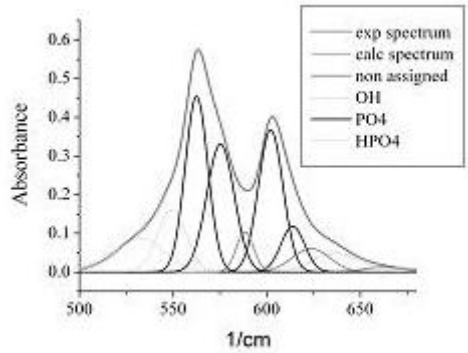

Fig. 3c – Experimental and calculated spectra of sample CO2 in the PO_4^{3-} bending mode ν_4 region.

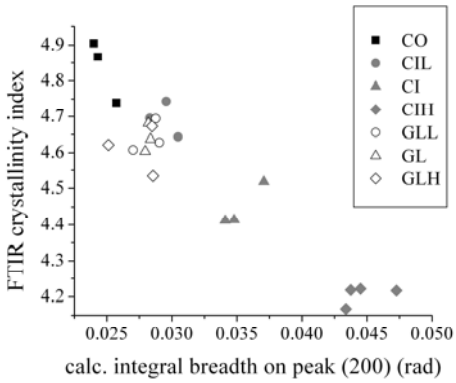

Fig. 4 – Graphical correlation between FTIR crystallinity index and integral bredth of 002 diffraction peak calculated from the refined parameters of Popa model.

SAXS

T values are apparently reproducible. No correlation was found between SAXS *T* values and XRD and FTIR (Fig. 5a). Only a non linear relationship can be suggested, if one considers just CO samples and samples precipitated in the presence of citrate. This might be due either to an independent change in sample mineral volume fraction or related to the assumptions during Porod constant determination. The former is due to the fact that we assume a constant mineral volume fraction of 0.5 (Hiller & Wess, 2006), while this value is likely to vary from sample to sample. The latter refers to the sample polydispersity: in this case background subtraction and Porod constant determination aren't straightforward, and personal interpretation can seriously affect data analysis.

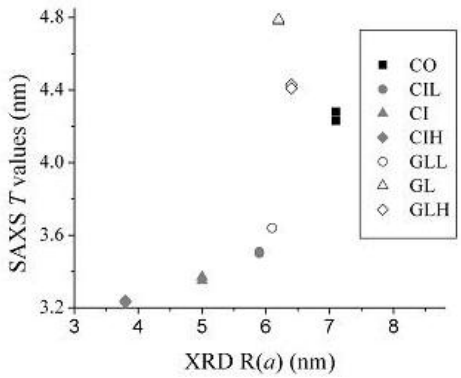

Fig. 5a – SAXS T values *vs.* XRD dimension along *c* as calculated from Popa parameters obtained from Rietveld refinements.

Scaled G(*x*) SAXS curves as defined in eq. 5 are shown in Fig. 5b. The curve profiles are compatible with crystals that are polydisperse in shape. A downwards shift of G(*x*) values at low *x* in the presence of high concentrations of citrate could suggest a certain control on the shape of the precipitating crystals. However any comparison between curves of polydisperse samples should be avoided.

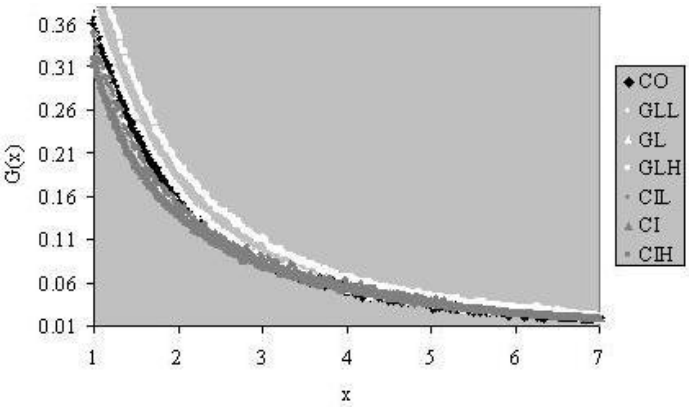

Fig. 5b – Scaled G(*x*) SAXS curves as defined in equation 2.5.8 from collected data. The profiles are compatible with polydisperse crystals.

CONCLUSIONS AND FUTURE WORK

The presence of both citrate and glutamate has been confirmed to affect the size, strain and crystallinity of HAp. The Rietveld refinement of XRD data can be used to quantify the changes in the size and strain of nanocrystalline HAp. We found a strong correlation between the FTIR crystallinity index and the XRD-determined broadening along the *a* axis for the samples here studied. In particular crystallinity along the *a* axis decreases as concentration of citrate increases. On the other hand, while lower crystallinity values were observed for HAp synthesized in the presence of glutamate, with respect to the control sample, there was no detectable effect relating to the concentration of the glutamate ligand.

FTIR analysis revealed CO_3^{2-} and HPO_4^{2-} substitution for phosphate and citrate surface complex presence.

No correlation between SAXS thickness values and XRD R(*a*) calculated from Popa model size parameters was found. This may simply relate to incorrect parameterization within the initial analyses of the SAXS data: it is not possible to estimate a range of values for the mineral volume fraction. Hiller & Wess (2006) use the same volume fraction value (0.5) as a constant for recrystallized archaeological bones. They seem to consider *T* as a variable of both thickness and volume fraction, avoiding a definitive interpretation. In this study SAXS analysis can only be used as a side technique. However further study of the SAXS technique to improve its role in this kind of application is required.

REFERENCES

Biltz, R.M. & Pellegrino, E. (1969): The chemical anatomy of bone - A comparative study of bone composition in sixteen vertebrates. *J. Bone Joint Surg. Am.*, **51**, 456-466.

Boanini, E., Torricelli, P., Gazzano, M., Giardino, R., Bigi, A. (2006): Nanocomposites of hydroxyapatite with aspartic acid and glutamic acid and their interaction with osteoblast-like cells. *Biomaterials*, **27**, 4428-4433.

Brecevic, L. & Furedi-Milhofer, H. (1979): Precipitation of calcium phosphates from electrolyte solutions V. The influence of citrate ions. *Calcif. Tissue Int.*, **28**, 131-136.

Elliott, J.C. (2002): Calcium phosphate biominerals. *Rev. Mineral. Geochem.*, **48**, 427-453.

Ferraz, M.P., Monteiro, F.J., Manuel, C.M. (2004): Hydroxyapatite nanoparticles: a review of preparation methodologies. *J. Appl. Biomat.*, **2**, 74-80.

Filgueiras, M.R.T., Mkhonto, D., de Leeuw, N.H. (2006): Computer simulations of the adsorption of citric acid at hydroxyapatite surfaces. *J. Cryst. Growth*, **294**, 60-68.

Fratzl, P., Schreiber, S., Klaushofer, K. (1996a): Bone mineralization as studied by small-angle X-ray scattering. *Connect. Tissue Res.*, **34**, 247-254.

Fratzl, P., Schreiber, S., Boyde, A. (1996b): Characterization of bone mineral crystals in horse radius by small-angle X-ray scattering. *Calcif. Tissue Int.*, **58**, 341-346.

Gross, K.A. & Berndt, C.C. (2002): Biomedical application of apatites. *Rev. Mineral. Geochem.*, **48**, 631-672.

Hiller, J.C. & Wess, T.J. (2006): The use of small-angle X-ray scattering to study archaeological and experimentally altered bone. *J. Archaeol. Sci.*, **33**, 560-572.

Hunter, G.K., Hauschka, P.V., Poole, A.R., Rosenbergs, L.C., Goldberg, H.A. (1996): Nucleation and inhibition of hydroxyapatite formation by mineralized tissue proteins. *Biochem. J.*, **317**, 59-64.

Lackovic, K., Johnson, B.B., Angove, M.A., Wells, J.D. (2003): Modeling the adsorption of citric acid onto Muloorina illite and related clay minerals. *J. Colloid Interf. Sci.*, **267**, 49-59.

Landi, E., Tampieri, A., Celotti, G., Vichi, L., Sandri, M. (2004): Influence of synthesis and sintering parameters on the characterics of carbonate apatite. *Biomaterials*, **25**, 1763-1770.

Lutterotti, L. (2006): MAUD tutorial – Instrumental broadening determination. http://www.ing.unitn.it/~maud/Tutorial/sizestrain/InstrumentalBroadening.pdf.

Matsumoto, T., Okazaki, M., Inoue, M., Hamada, Y., Taira, M., Takahashi, J. (2002): Crystallinity and solubility characteristics of hydroxyapatite adsorbed amino acid. *Biomaterials*, **23**, 2241-2247.

Pang, Y.X. & Bao, X. (2003): Influence of temperature, ripening time and calcination on the morphology and crystallinity of hydroxyapatite nanoparticles. *J. Eur. Ceram. Soc.*, **23**, 1697-1704.

Popa. N.C. (1998): The (*hkl*) dependence of diffraction-line broadening caused by strain and size for all Laue groups in Rietveld refinement. *J. Appl. Crystallogr.*, **31**, 176-180.

Porod, G. (1982): General theory. *In*: "Small angle X-ray scattering", O. Glatter & O. Kratky, eds. Academic Press, New York, 17-51.

Rey, C., Renugopalakrishnan, V., Collins, B., Glimcher, M.J. (1991): Fourier transform infrared spectroscopic study of the carbonate ions in bone mineral during aging. *Calcif. Tissue Int.*, **49**, 251-258.

Rodrìguez-Lorenzo, L.M. & Vallet-Regì, M. (2000): Controlled crystallization of calcium phosphate apatites. *Chem. Mater.*, **12**, 2460-2465.

Sàenz, A., Montero, M.L., Mondragòn, G., Rodrìguez-Lugo, V., Castano, V.M. (2003): Effect of *p*H on the precipitation of hydroxyapatite on silica gels. *Mat. Res. Innovat.*, **7**, 68-73.

Surovel, T.A. & Stiner, M.C. (2001): Standardizing infra-red measures of bone mineral. *J. Archaeol. Sci.*, **28**, 633-642.

Tsortos, A. & Nancollas, G.H. (2002): The role of polycarboxylic acids in calcium phosphate mineralization. *J. Colloid Interf. Sci.*, **250**, 159-167.

Van der Houwen, J. (2003): Chemical principles of calcium phosphate dissolution and precipitation. PhD thesis, University of Reading.

Van der Houwen, J., Cressey, G., Cressey, B.A., Valsami-Jones, E. (2003): The effect of organic ligands on the cristallinity of calcium phosphate. *J. Cryst. Growth*, **249**, 572-583.

Wang, A., Yin, H., Liu, D., Wu, H., Ren, M., Jiang, T., Cheng, X., Xu, Y. (2006): Size-controlled synthesis of hydroxyapatite nanorods in the presence of organic modifiers. *Mater. Lett.*, **61**, 1341-1345.

Weng, W., Han, G., Du, P., Shen, G. (2002a): The effect of citric acid addition on the formation of sol–gel derived hydroxyapatite. *Mater. Chem. Phys.*, **74**, 92-97.

Weng, W., Han, G., Du, P., Shen, G. (2002b): The effect of citric acid addition on sol–gel preparation of apatite films. *Mater. Chem. Phys.*, **77**, 578-582.

Wright, L.E. & Schwartz, H.P. (1996): Infrared and isotopic evidence for diagenesis of bone apatite. *J. Archaeol. Sci.*, **23**, 933-944.